

## Tripping Instability of Ring Stiffened Cylinders induced by Underwater Explosions

Y.O. Shin<sup>1</sup> and Y.S. Shin<sup>2</sup>

<sup>1</sup>Daewoo Shipbuilding & Marine Engineering Co., Ltd.  
Seoul, South Korea

<sup>2</sup>Ocean Systems Engineering Division  
Korea Advanced Institute of Science and Technology, Daejeon, South Korea

### Abstract

The dynamic stability of a ring-stiffened cylindrical hull structure subjected to underwater explosion is investigated using a finite element approach. The arbitrary Lagrangian-Eulerian (ALE) method in LS-DYNA is employed for the analysis. One of the detrimental collapse instabilities in tripping is identified in the ring stiffened cylindrical structure. Tripping can be defined as lateral-torsional buckling behaviour of the ring stiffener. The stiffener tripping-form of collapse is a sudden and drastic reduction in load-carrying ability resulting in total failure.

Progressive tripping phenomenon is observed to identify the triggering instability that causes total collapse. Sensitivity analysis is conducted to investigate the region that is unstable with respect to stiffener tripping. The stability region is proposed in terms of ring-stiffener sizing with respect to hull structure configuration.

**Keywords:** underwater explosion, arbitrary Lagrangian-Eulerian method, tripping.

## 1 Introduction

Underwater explosion (UNDEX) is a highly important and complex problem for naval surface ships and submarines. Detonating high explosives in underwater generates a shock wave and a pulsating gas bubble. The dynamic responses of submerged structures impinged upon by UNDEX have received considerable attention since the 1950s. When UNDEX occurs within the vicinity of the structure, structure deformation occurs because of the tripping phenomenon. This phenomenon, which pertains to lateral-torsional buckling, is serious problem that contributes to the damage response of submerged structures.

In this study, sensitivity analysis is conducted to observe the progressive tripping and identify the triggering instability that causes total collapse. On the basis of the result, the region that is stable against tripping throughout the parametric study is proposed. Two types of the submerged structure investigated are the rectangular ring

stiffened cylindrical shell and tee ring stiffened cylindrical shell with hemispherical end caps. This model was simulated to study the dynamic behavior of structure instead of the physical testing since the physical testing of submerged structure subjected to underwater explosion is enormous cost and limited by environmental concern.

The response of structure is calculated by Arbitrary Lagrangian-Eulerian method (ALE). ALE is used to the fluid-structure interaction and LS-DYNA is used to analyze the structure subjected to UNDEX.

## 2 Theoretical background

### 2.1 Shock loading

The rate of energy release during the detonation process results in greater destructive power. At very early times the gas pressure acts on the surrounding water, thereby resulting in the compression and radial motion of the water. Thus, a shock wave is generated and emitted. Shock wave velocity steadily increases within the explosive until velocity exceeds the speed of sound in the explosive. About 53% of the energy of the explosion energy is transmitted in the shock wave and about 47% of the explosion energy generates a gas bubble.

The UNDEX pressure equation proposed by Cole [1] can be expressed as follows;

$$P(t) = P_{max}e^{-t/\theta}, t \geq t_1 \quad (1)$$

This shock formula is empirically determined as the equation of pressure history. It is accurate at a distance of 10 to 100 radius of the explosive, where  $P_{max}$  is the peak pressure (pa) in the shock front,  $t$  is the time elapsed after the arrival of the shock (ms), and  $\theta$  denotes the exponential decay time constant (ms) which is a good approximation of the pressure that is greater than one-third of the peak pressure value [1].

$$P_{max} = 2315.883K_1 \left(\frac{W^{1/3}}{R}\right)^{A_1} \text{ (pa)} \quad (2)$$

$$\theta = 1.544K_2 W^{\frac{1}{3}} \left(\frac{W^{1/3}}{R}\right)^{A_2} \text{ (ms)} \quad (3)$$

The empirical equation of the maximum bubble radius ( $A_{max}$ ) and gas bubble period (T) can be expressed as follows;

$$A_{max} = 0.397K_6 \frac{W^{1/3}}{(3.208D+33)^{1/3}} \text{ (m)} \quad (4)$$

$$T = 1.3K_5 \frac{W^{1/3}}{(3.208D+33)^{5/6}} \text{ (s)} \quad (5)$$

where  $K_1, K_2, K_3, K_4, K_5, A_1$  and  $A_2$  are constants that depend on charge type (Table 1).  $R$  (in m) is the distance between the explosive charge and target and  $D$  denotes the depth (in m) of the explosive.  $W$  represents the weight of the explosive charge in lb. This empirical equation result is satisfied at a depth is between 50% and 80% of the maximum radius [2].

Description	Parameter	Explosive type		
		HBX-1	TNT	PETN
$P_{\max}$	$K_1$	22,347.6	22,505	24,589
	$A_1$	1.144	1.18	1.194
Decay constant	$K_2$	0.056	0.058	0.052
	$A_2$	-0.247	-0.185	-0.257
Bubble period	$K_5$	4.761	4.268	4.339
Bubble radius	$K_6$	14.14	12.67	12.88

Table 1: Shock wave parameter value.

## 2.2 Arbitrary Lagrangian-Eulerian Method

In choosing a solution method for simulating problems, an appropriate kinematical description of the continuum is a fundamental consideration.

In the Lagrangian approach, the computational mesh follows the associated material particle during motion. The Lagrangian description enables the easy tracing of free surfaces and interfaces between different materials. Its weakness is its inability to follow large distortions of the computational domain without resorting to frequent remeshing operations [3, 4].

In the Eulerian approach, the computational mesh is fixed using the Navier-Stokes equation and the continuum moves with respect to the grid. The Eulerian description large distortions in the continuum motion can be handled with relative ease, but generally at the expense of precise interface definition and resolution of flow details [3, 4].

To compensate for the shortcoming of a purely Lagrangian and purely Eulerian description, another approach that combines the best features of the two has been developed. In this approach, called the ALE method, the nodes of the computational mesh may move with the continuum in normal Lagrangian fashion, be fixed in an Eulerian manner or move in some arbitrary specified manner to yield a continuous rezoning capability. Because of the freedom offered by the ALE description in moving the computational mesh, greater distortions of the continuum can be handled than is possible using a purely Lagrangian method, and with more resolution than is afforded by a purely Eulerian approach.

The numerical analysis conducted in this study features an ALE finite element code. LS-DYNA is used for the numerical analysis in this investigation. ALE hydrocodes use both Lagrangian and Eulerian hydrocodes that perform automatic rezoning. An ALE hydrocode involves a Lagrangian time step followed by a remap or advection phase [3, 4].

## 2.3 Tripping

The submarine ring-stiffened cylinder is designed with generous safety margins against overall collapse triggered by frame yielding or tripping. Tripping or lateral-torsional buckling occurs when the stiffeners rotate about the line of attachment to the plating. Figure 1 illustrates the tripping phenomenon.

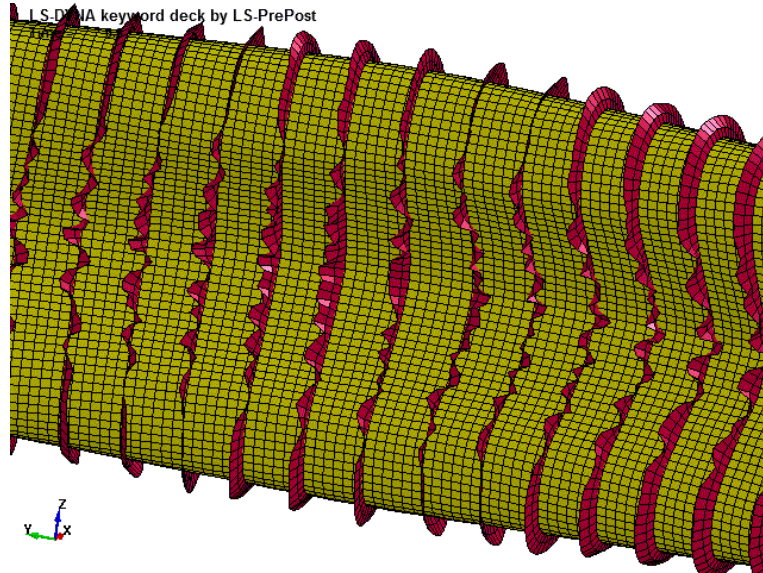


Figure 1: Stiffener tripping.

Stiffener tripping is regarded as panel collapse, because when tripping occurs the plating is left with no stiffening and collapse follows immediately. This type of buckling is caused by a high resistance to bending in one plane and low resistance to bending in another, imperfections in the beam, and a sufficiently large force pushing in a direction perpendicular to the beam's large moment of inertia. Tripping is induced by three equilibrium equations: one equation associated with strong axis bending; one equation associated with weak axis bending, and one equation associated with twisting.

To simply find the critical value for tripping, this study assume that lateral-torsional buckling is a simply-supported beam of length  $L$  and doubly-symmetric cross-section under a uniform bending moment  $M$  to determine the critical value of  $M = M_{crit}$  [5].

The cross-section is assumed to be doubly-symmetric with second moments of area:  $I_x$ (major axis),  $I_y$ (minor axis); St Venant torsion constant:

$$J = \sum[\text{breadth} \times (\text{thickness})^3]/3 \quad (6)$$

Young's modulus:  $E$  ; Poisson's ratio:  $\nu$  ; and shear modulus:  $G = E/[2(1 + \nu)]$ . Figure 2 shows the displacement of the cross-section with its combination of twisting and lateral movement [5].

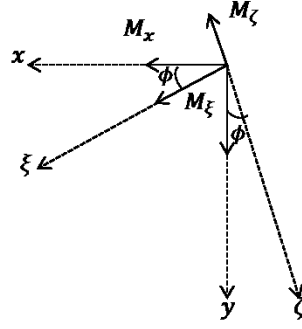


Figure 2: Section twisting and moving laterally.

With the angle of twist  $\phi$ , the lateral displacement  $u$  and the vertical displacement  $v$ . For the assumed small displacements  $\cos \phi \approx 1$  and  $\sin \phi \approx \phi$ . We can first say that the bending moment about the major axis is  $M_x = M$  and about the minor axis  $M_y = \phi M$ . Then the following differential equations can be written from bending theory: [5]

$$EI_x \frac{d^2 v}{dz^2} = M \quad (7)$$

$$EI_y \frac{d^2 u}{dz^2} = \phi M \quad (8)$$

The internal moment of torsion consists of a warping and uniform torsion component.

The torsion arising from the angle of twist  $\phi$  is not uniform because of section warping. The equation for non-uniform torsion is given by:

$$GJ \frac{d\phi}{dz} - EI_w \frac{d^3 \phi}{dz^3} = T \quad (9)$$

where the second term in Eqn. (9) is the correction for warping with  $T$  being the induced torque from the external bending moment  $M$  and the change in lateral displacement  $u$  along the beam (in  $z$  direction) and  $I_w$  is called the *warping stiffness* ( $\text{mm}^6$ ) which is equal to  $I_y h^2 / 4$  for an I-section, where  $h$  is the section height. The Eqn. (7) gives the following governing differential equation for  $\phi$  in terms of  $z$

$$EI_w \frac{d^4 \phi}{dz^4} - GJ \frac{d^2 \phi}{dz^2} - \frac{M^2 \phi}{EI_y} = 0 \quad (10)$$

Substituting the second solution into Eqn. (9) and solving the resulting quadratic equation in  $M$  gives the expression of the critical moment: [5]

$$M_{crit} = \frac{\pi}{L} \sqrt{EI_y GL} \sqrt{1 + \frac{\pi^2 EI_w}{L^2 GJ}} \quad (11)$$

As the name suggests, lateral torsional buckling is a phenomenon including both out of plane buckling and twisting of the cross-section. This leads to a beam displacement that includes contribution from lateral displacement and the angle of twist.

The twisting of the cross-section includes components of warping torsion and St Venant's torsion. And the resistance of the cross-section to this twisting is dependent on  $I_w$ , the warping constant, and  $J$ , the St Venant's torsion and the polar moment of inertia.

The critical moment of the cross-section will vary based on the end restraint, the moment gradient, and the placement of the load.

## 2.4 Effective plastic strain (EPS)

To calculate the plastic strains, three properties are used to characterize the material behavior;

A yield function, which gives the yield condition that specifies the state of multiaxial stress corresponding to start of plastic flow

A flow rule, which relates the plastic strain increments to the current stresses and the stress increments

A hardening rule, which specifies how the yield function is modified during plastic flow

The yield function has the general form at time  $t$ ,

$${}^t f_y(\sigma_{ij}, {}^t e_{ij}^P, \dots) \quad (12)$$

Where "... .." denotes state variables that depend on the material characterization. The instantaneous material response is elastic if

$${}^t f_y < 0 \quad (13)$$

and elastic or plastic depending on the loading condition if

$${}^t f_y = 0 \quad (14)$$

whereas  ${}^t f_y > 0$  is inadmissible. Hence the relation Eqn.(14) represents the yield condition, which must hold throughout the plastic response.[6]

Assuming that for the material the associated flow rule is applicable during plastic response the function  ${}^t f_y$  in the flow rule is used to obtain the plastic strain increments

$$de_{ij}^P = d\lambda \frac{\partial {}^t f_y}{\partial {}^t \sigma_{ij}} \quad (15)$$

where  $d\lambda$  is scalar to be determined.

Effective plastic strain is follows;

$${}^{t+\Delta t}\bar{e}^P = \int_0^{t+\Delta t} \sqrt{\frac{2}{3} de^P \cdot de^P} \quad (16)$$

Effective plastic strain is a monotonically increasing scalar value which is calculated incrementally as a function of  $de_{ij}^P$ , the plastic component of the rate of deformation tensor Eqn.(16). It grows whenever the material is actively yielding, i.e., whenever the state of stress is on the yield surface.[6]

### 3 Numerical model description

#### 3.1 Simulation

The fluid and structure model are created using TrueGrid software and then are exported to LS-DYNA code to analyze the transient dynamic behavior. Fig. 20 depicts a stiffened cylindrical structure with a depth of 150 m, subjected to shock wave induced by 65 kg TNT detonated 1 m away from the side of the structure. The total simulation time is 0.5 s but the explosive charge explodes at 0.2 s because the hydrostatic pressure is stabilized for 0.2 s. The time step is  $1.0 \times 10^{-5}$  s, which is acceptable for the mesh size of this model.

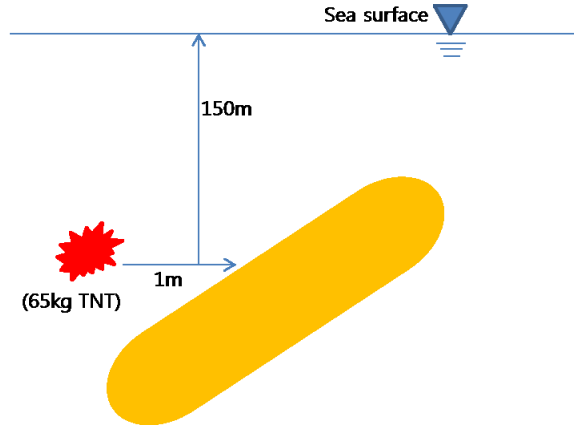


Figure 3: Scenarios of simulation

#### 3.2 Water and air model

Figure.4 show the water model with a depth, width and height of 120 m. The water density is  $1025 \text{ kg/m}^3$ . The equation of state (EOS) is calculated by the linear polynomial equation of state which is expressed as, [7]

$$P = C_0 + C_1 + C_2\mu^2 + C_3\mu^3 + (C_4 + C_5 + C_6\mu^2)E \quad (17)$$

The initial pressure of EOS is determined by multiplying the  $C_4$  and  $E$ . For the condition of 150 m water depth, the initial pressure of EOS was changed. The water

model contains 3242648 solid elements. The mesh size at the region which contains the structure model and the TNT model is fine to reduce the effect of reflection wave and perform the accurate bubble motion.

The air is inside the stiffened cylindrical structure (Figure 4). The density of air is  $1.22 \text{ kg/m}^3$ . The EOS is calculated by Eqn. (17). The values of the linear polynomial equation of state are presented in Table 2.

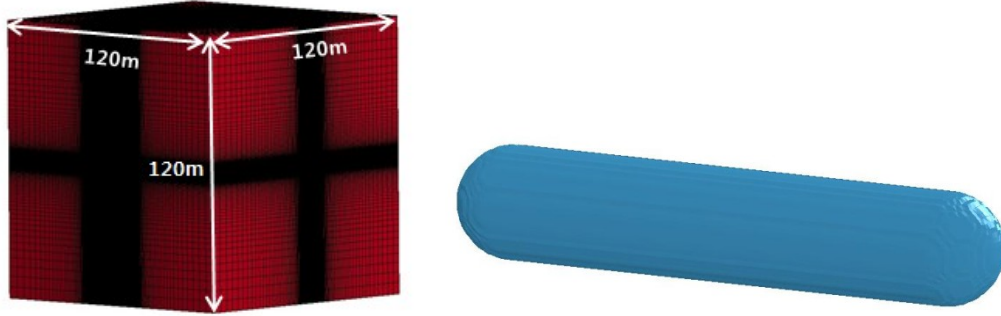


Figure 4: Water and air model

	Linear polynomial EOS							E(J/m <sup>3</sup> )
	C <sub>0</sub>	C <sub>1</sub> (Pa)	C <sub>2</sub>	C <sub>3</sub>	C <sub>4</sub>	C <sub>5</sub>	C <sub>6</sub>	
Sea water	0	2.036E+9	8.432E+9	0.14E+9	0.4934	1.3937	0	2.280E+5
Air	0	1.010E+5	0	0	0.4	0.4	0	2.533E+5

Table 2: Linear polynomial EOS

### 3.2 Explosive model

Figure 5 shows the explosive model which is in the center of water. The density of explosive is  $1630 \text{ kg/m}^3$ . The EOS is calculated by The JWL of equation of state which defines pressure as a function of relative volume,  $V$ , and internal energy per initial volume,  $E$ , as [7]

$$P = A \left(1 - \frac{\omega}{R_1 V}\right) e^{-R_1 V} + B \left(1 - \frac{\omega}{R_2 V}\right) e^{-R_2 V} + \frac{\omega E}{V} \quad (18)$$

Where  $\omega$ ,  $A$ ,  $B$ ,  $R_1$ , and  $R_2$  are input parameters.

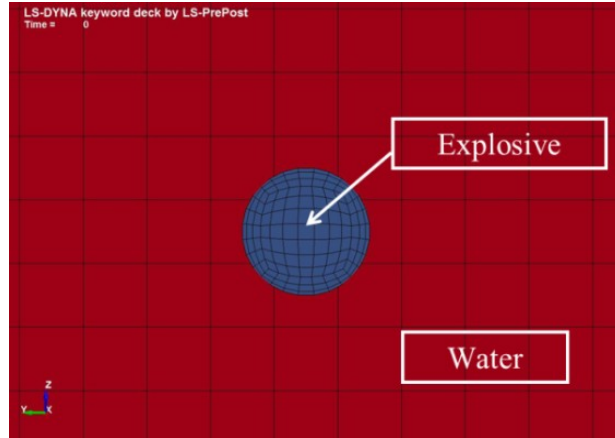


Figure 5: Explosive model

### 3.3 Rectangular ring-stiffened cylindrical structure

The cylindrical shell is reinforced by equally spaced rectangular-type ring stiffener and two hemispherical shell end caps. The dimensions of the basic model are shown in Table 3. These structural dimensions are based on [8]. Figure 6 shows rectangular ring-stiffened cylindrical structure model

We perform a parametric study by varying the standard ring stiffener thickness and height which are shown in Table 4.

Cylindrical shell			Rectangular stiffener		
Radius (m)	Length (m)	Thickness (m)	Height (m)	Thickness (m)	Spacing (m)
5.0 m	21.6 m	0.024 m	0.17 m	0.009 m	0.9 m

Table 3: Dimension of the basic rectangular stiffened cylindrical structure

Changes in ring stiffener height		Changes in ring stiffener thickness	
Model	Height	Model	Thickness
WH_34	0.34 m	WT_34	0.034 m
WH_23	0.23 m	WT_18	0.018 m
WH_17	0.17 m	WT_13.5	0.0135 m
WH_11	0.11 m	WT_9	0.009 m
WH_8.5	0.085 m	WT_6.6	0.0066 m
WH_7.5	0.075 m	WT_4.5	0.0045 m

Table 4: Changes in ring stiffener dimensions

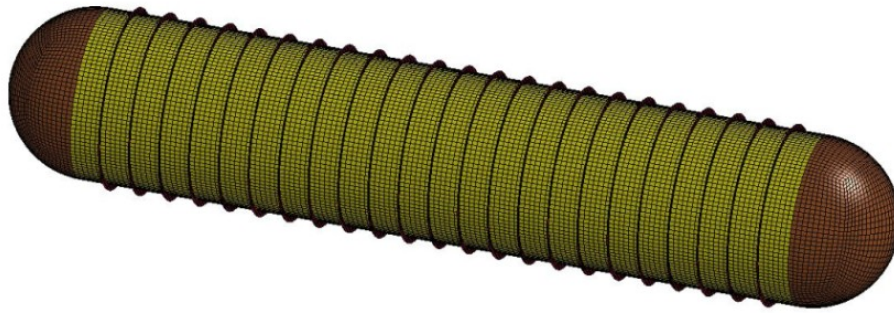


Figure 6: Rectangular ring stiffened cylindrical structures.

### 3.4 Tee ring-stiffened cylindrical structure

The cylindrical shell and two hemispherical shells have the same as those of the rectangular ring-stiffened cylindrical shell. The dimensions of the basic tee ring stiffener model are shown Table 5. Figure 7 shows the tee ring-stiffened cylindrical structure.

For tee ring-stiffened cylindrical structure, three parametric studies are conducted to determine the region that is stable against tripping. One of the parametric studies is performed by changing the height of the web. The other involves is varying the width of the flange and the last study is conducted by changing the thickness of the flange (See Table 6).

Tee ring stiffener			
Web height	Web & Flange thickness	Flange width	Spacing
0.17 m	0.009 m	0.17 m	0.9 m

Table 5: Basic tee ring stiffener

Changes in web height		Changes in flange width		Changes in flange thickness	
Model	Height	Model	Width	Model	Thickness
FH_34	0.34 m	FB_34	0.34m	FT_18	0.018m
FH_23	0.23 m	FB_23	0.23m	FT_13.5	0.0135m
FH_17	0.17 m	FB_17	0.17m	FT_9	0.009m
FH_11	0.11 m	FB_11	0.11m	FT_6.5	0.0065m
FH_8.5	0.085 m	FB_8.5	0.085m	FT_4.5	0.0045m

Table 6: Changes in tee ring stiffener dimensions



Figure 7: Tee ring-stiffened cylindrical structure

### 3.5 Material properties of structure

The cylinder hull and ring stiffener are made of HY-100 steel and modeled in plastic kinematic material mode so that they can endure the dynamic load provided by the high hydraulic pressure and shockwave. HY-100 steel-quenched and tempered low-carbon alloy steel finds uses as pressure vessels, heavy construction equipment, and in large steel structures. HY-100 steel has good ductility, high tensile strength, notch stiffness, weld ability and corrosion resistance. The material properties of the HY-100 steel are shown in Table 7.

Yield strength ( $\sigma_y$ )	Young's modulus (E)	Ultimate strength ( $\sigma_U$ )	Density ( $\rho_s$ )	Poisson's ratio ( $\mu$ )
690 MPa	205 GPa	793.5 MPa	7870 kg/m <sup>3</sup>	0.28

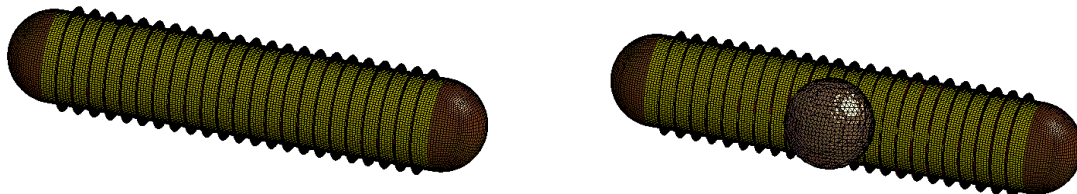
Table 7. Properties of HY-100

## 4 Numerical analysis

### 4.1 Rectangular ring stiffener

#### 4.1.1 Simulation of the rectangular ring stiffener

The sequences of bubble motion and cylindrical shell behavior are illustrated in Figure 8 and Stiffener tripping is shown in Figure 9.



(a) Simulation at 0.0 sec

(b) Simulation at 0.25 sec

Figure 8: (continued) Motion of the rectangular ring stiffened cylindrical structure

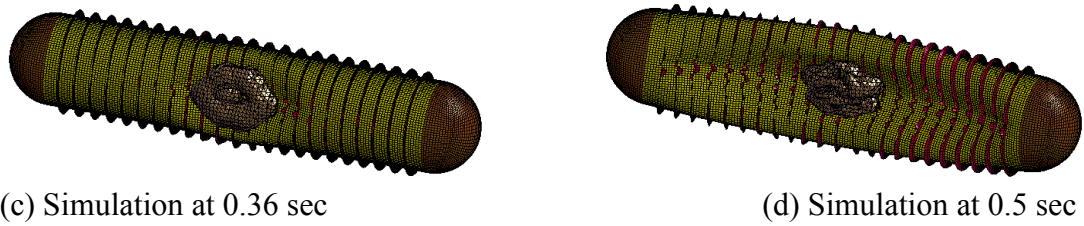


Figure 8: (continued) Motion of the rectangular ring stiffened cylindrical structure

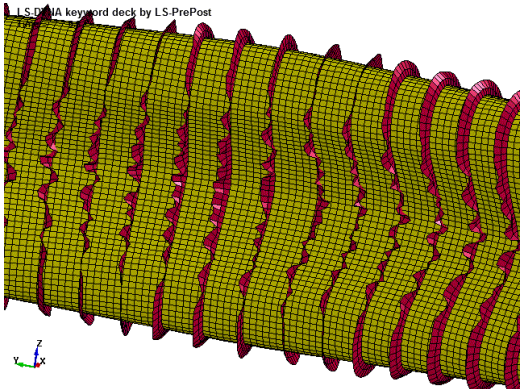


Figure 9: Tripping for rectangular ring stiffener

**4.1.2 EPS measure points for the rectangular ring stiffener**

To compare the deformation of the stiffener and cylinder, the EPS is measured at the particular elements of the model that are influenced by the shockwave pressure and bubble effect.

The particular elements of the model are shown in Figure 10. The element p1, p2 and p3 are used to measure the EPS of the plate while the others are to measure the EPS of the stiffener. The element p3 is at the middle of the structure.

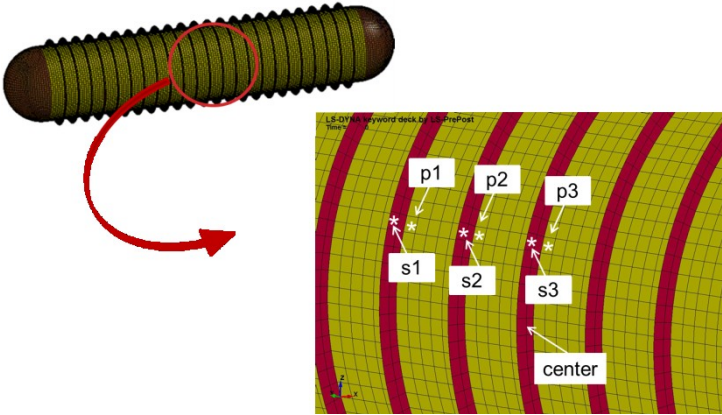


Figure 10: Measured elements of the model

### 4.1.3 Changing the height of the rectangular ring stiffener

The parametric studies on the change in web height, with web thickness kept constant, are performed to investigate tripping behavior and structure deformation.

The simulation cases are listed in Table 4. Figure 11 shows the variations in the EPS values of the stiffener with increasing  $h_w/t_w$  and constant stiffener web thickness. And Figure 12 shows the variation in the EPS values of the cylindrical shell.

As shown in Figure 11, determining the trend of tripping behavior for the stiffener is a difficult task.

Figure 11 implies that as the height of the stiffener web increases, the EPS values typically increase. Therefore, as the height of the stiffener increases, the deflection of the rectangular ring-stiffened cylindrical structure also increases.

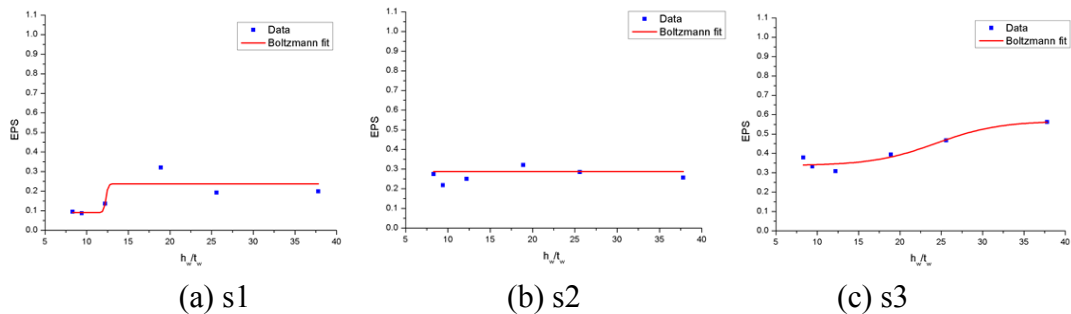


Figure 11: Variation of in the EPS values of the stiffener with increasing  $h_w/t_w$  and the stiffener web thickness kept constant.

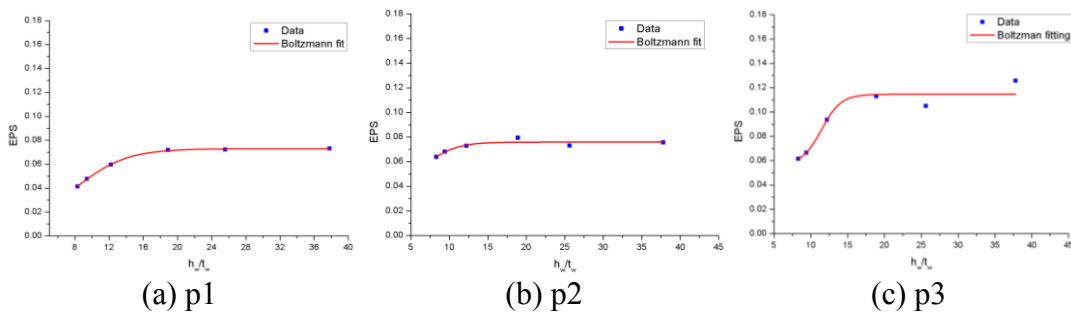


Figure 12: Variation of in the EPS values of the plate with increasing  $h_w/t_w$  k and stiffener web thickness kept constant.

### 4.1.4 Changing the thickness of the rectangular ring stiffener

The parametric studies on the change in web thickness, with web height kept constant, are performed to investigate tripping behavior and structure deformation. The simulation cases are listed in Table 4.

Figure 13 illustrates the variations in EPS values for the stiffener with increase  $h_w/t_w$  and constant stiffener web height. And Figure 14 shows the variation in the EPS values of the cylindrical shell.

Figure 13 and Figure 14 indicate that increasing the thickness of the stiffener web effectively diminishes the possibility of tripping and deformation of cylindrical shell.

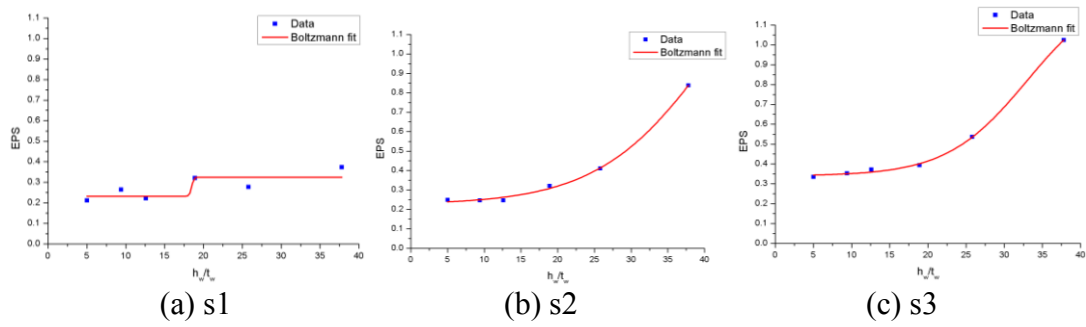


Figure 13: Variation in the EPS values of the stiffener with increasing  $h_w/t_w$  and the stiffener web height kept constant.

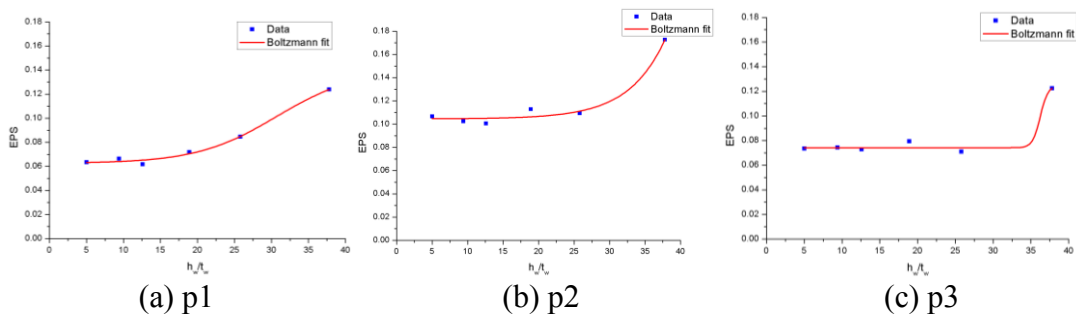


Figure 14: Variations in the EPS for the plate with increasing  $h_w/t_w$  and constant stiffener web height.

## 4.2 Tee ring stiffener

### 4.2.1 Simulation of the tee ring stiffener

The stiffener tripping is shown in Figure 15.

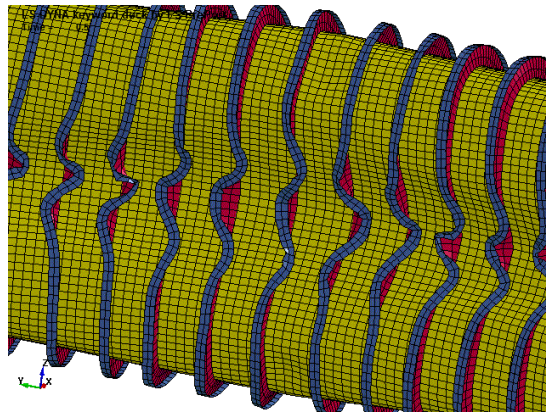


Figure15: Tripping for tee ring stiffener

#### 4.2.2 Changing the web height of the tee ring stiffener

The EPS is measured at particular elements of the flange and cylinder which are affected by the shockwave pressure and bubble effect.

Elements f1, f2 and f3 are measured to compare the deformations of the stiffener.

Elements p1, p2 and p3 are measured to compare the deformations of the cylinder.

The measured elements for the cylinder are the same as those measured for the rectangular ring-stiffened cylindrical shell. The elements for the flange and cylinder are shown in Figure 16.

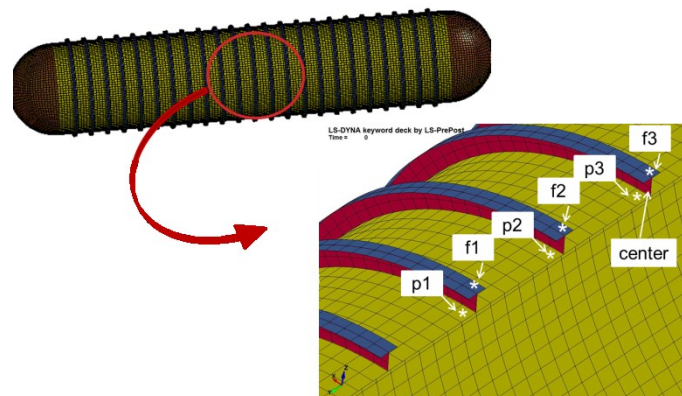


Figure 16: Measured elements of the model for the tee ring-stiffened cylindrical structure

#### 4.2.3 Changing the web height of the tee ring stiffener

The parametric studies are performed by varying the height of the stiffener web, with the web thickness, flange width and flange thickness kept constant to investigate stiffener tripping behavior and cylinder deformation. The simulation cases are listed in Table 5.

Figure 17 show the variations in the EPS values of the stiffener with creasing  $h_w/b_f$  and constant the web thickness, flange thickness and flange width. Figure 18 shows the variations in the EPS values of the cylinder with increasing  $h_w/b_f$  and constant web thickness, flange thickness and flange width to compare the degrees of deformation of the cylinder. Figure 17 and 18 clearly show that increasing the height of the web results in obvious tripping behavior and cylinder deformation.

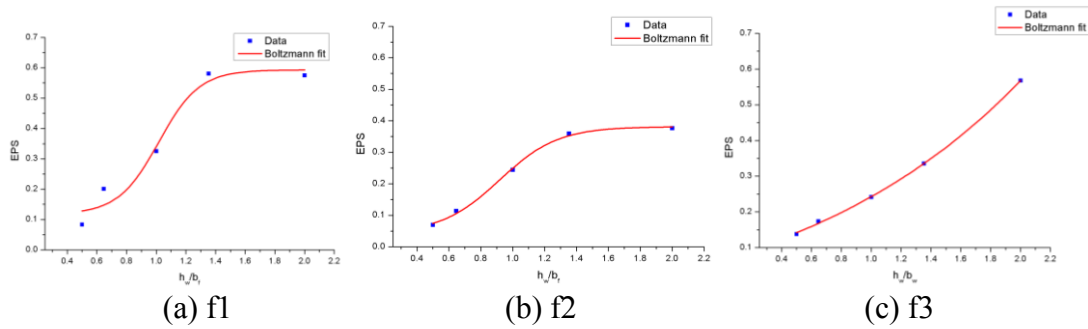


Figure 17: Variation in the EPS values of the stiffener with increasing  $h_w/b_f$  and constant web thickness, flange thickness and flange width.

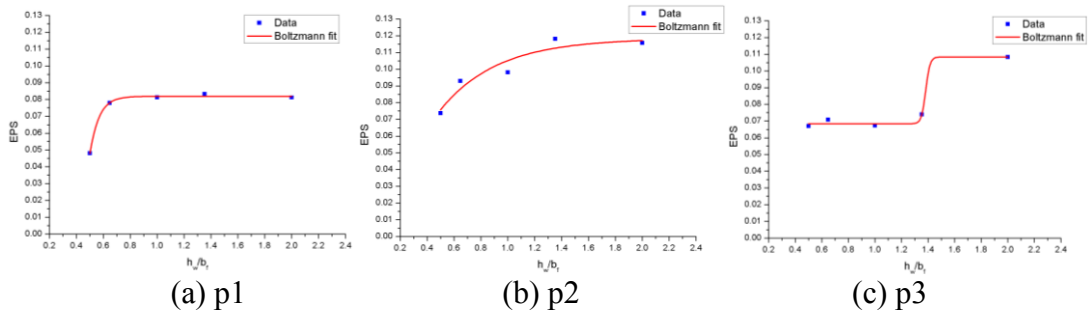


Figure 18: Variations in the EPS value of the cylindrical structure with increasing  $h_w/b_f$  and constant web thickness, flange thickness and flange width.

#### 4.2.4 Changing the flange width of the tee ring stiffener

Figure 19 shows the variations in the EPS values of the stiffener with increasing  $h_w/b_f$  and constant web thickness, web height, and flange thickness. Figure 20 presents the variations in the EPS values of the cylinder with increasing in  $h_w/b_f$  and constant web thickness, height, and flange thickness.

The determining the trend of stiffener tripping by varying the flange of width is difficult to accomplish.

Figure 20 shows the trend that increasing the width of the flange increases deformation of the cylinder.

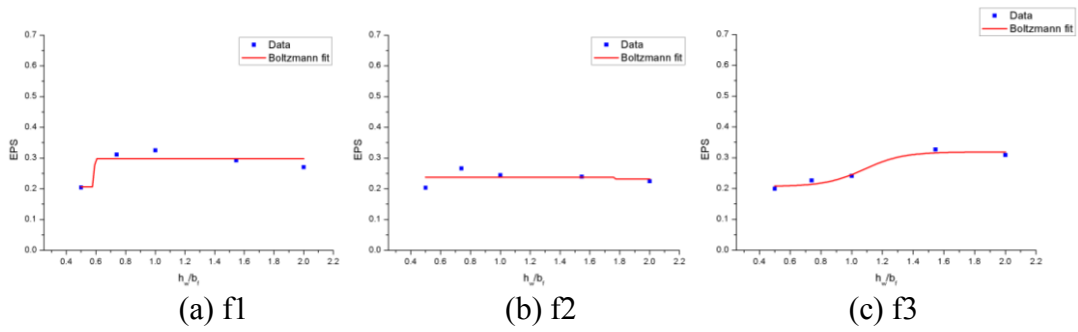


Figure 19: Variations in the EPS values of the stiffener with increasing  $h_w/b_f$  and constant web thickness, web height and flange thickness

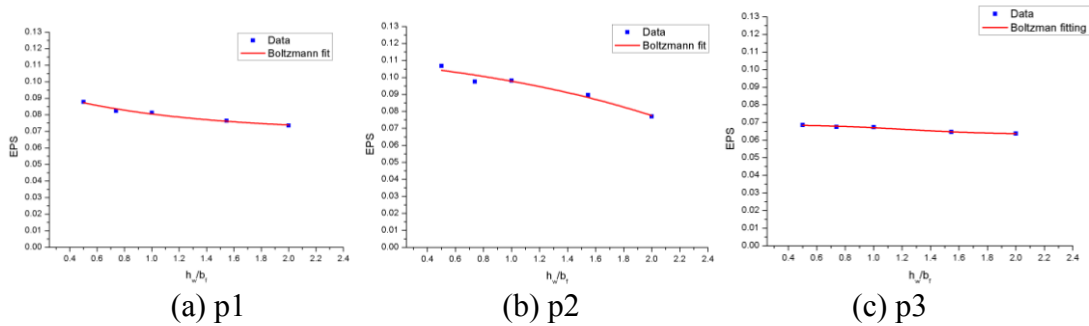


Figure 20: Variation in the EPS values of the cylindrical structure with increasing  $h_w/b_f$  and constant the web thickness, web height and flange thickness.

#### 4.2.5 Changing the flange thickness of the tee ring stiffener

Figure 21 shows the variations in the EPS values of the stiffener with increasing flange thickness and constant web thickness, web height, and flange width. Figure 22 presents the variations in the EPS values of the cylinder with increasing in flange thickness and constant web thickness, height, and flange width.

As the thickness of the flange increases, stiffener tripping and cylinder deformation decrease

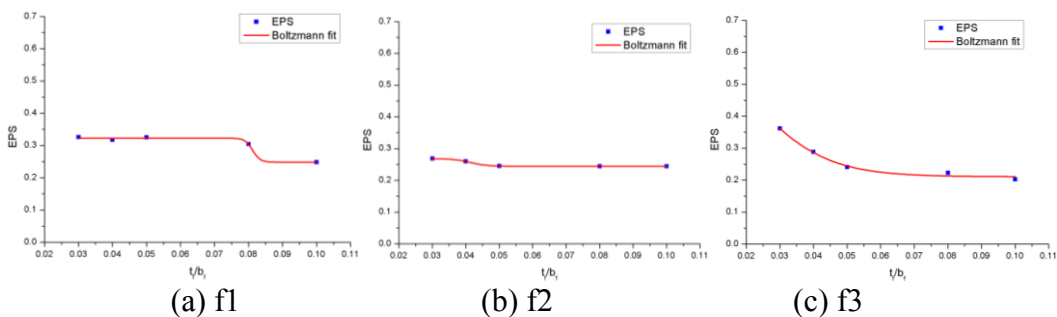


Figure 21: Variations in the EPS of the stiffener with increasing flange thickness and constant the web thickness, web height, and flange width.

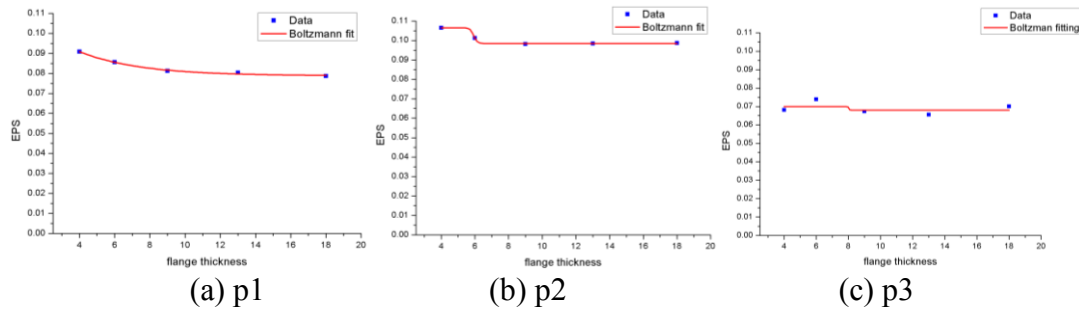


Figure 22: Variations in the EPS value of the cylindrical structure with increasing flange thickness and constant web thickness, web height and flange width.

## 5 Conclusion

This study has investigated the dynamic behavior of ring-stiffened cylindrical structure subjected to UNDEX. To identify for the region that is unstable against stiffer tripping and cylindrical shell deformation, parametric studies were performed using modelling and simulation. Two types of submerged structures were investigated: (1) a rectangular ring-stiffened cylindrical structure with hemispherical end caps and (2) a tee ring-stiffened cylindrical structure with hemispherical end caps. For the rectangular ring-stiffened cylindrical structure, two parametric studies were carried out: one of featured variation in web height, with constant web thickness, while the other involved changes in the thickness of the web, with web height kept constant. For the tee ring-stiffened cylindrical structure, three types of simulations were performed: the first involved changes in the web height, with web thickness, flange width, and flange thickness kept constant: the second featured variations in the flange width, with flange thickness, web height and web thickness kept constant: and the third involved change in the flange thickness, with flange width, web height and web thickness kept constant.

The results of the rectangular ring-stiffened cylindrical structure simulation show that varying web thickness is a better approach than changing web height in determining the tendency of tripping behaviour. Moreover, reducing web height more effectively reduces cylindrical structure deformation than does increasing web thickness.

The findings of the tee ring-stiffened cylindrical structure simulation indicate that flange width does not affect tripping behavior, but web height and flange thickness do. For cylindrical shell deformation of the cylindrical shell increases as web height rises. Decreasing the flange thickness, results in increased cylindrical shell deformation.

The possibility of cylindrical shell tripping and deformation is more sensitive to web height than to flange width and thickness.

## Acknowledgement

This research was supported by WCU (World Class University) program through the National Research Foundation of Korea funded by the Ministry of Education, Science and Technology (R31-2008-000-10045-0)

## Reference

- [1] Cole, R.H., “Underwater Explosions”, Princeton University Press, 1948
- [2] Shin, Y.S., “Ship shock modeling and simulation for far-field underwater explosion”, *Computers & Structure*, 82, 2211-2219, 2004
- [3] Mohamed, S., and David, J.B., “Arbitrary Lagrangian-Eulerian and Fluid-Structure Interaction”, John Wiley & Sons, Inc., New Jersey, 2010.
- [4] Donea, J., Huerta, A., Ponthot, J., and Rodriguez-Ferran, Q., “Arbitrary Lagrangian-Eulerian methods”, *Encyclopedia of Computational Mechanics*, 2004.
- [5] Theodore V.G., Andrea E.S., “Structural stability of steel: concepts and applications for structural engineers”, John Wiley & Sons, Inc, New jersey, 2008
- [6] Klaus-Jurgen Bathe, “Finite Element Procedures”, New jersey, United States of America, 1996.
- [7] LSTC, “LS/DYNA3D User’s Manual, Version 971”, Livermore Soft Technology Corp., 2007
- [8] Radha, P., and Rajagopabn, K., “Random Polar Sampling Technique for Reliability Analysis of submarine pressure hull”, *Journal of Naval Architecture and marine Engineering*, 2004.